Acta Materialia 246 (2023) 118704

Contents lists available at ScienceDirect

Acta Materialia

journal homepage: www.elsevier.com/locate/actamat

Full length article

Additive manufacturing of Al_2O_3 with engineered interlayers and high toughness through multi-material co-extrusion

Shitong Zhou [a,*], Qiaosong Cai [a], Iuliia S Tirichenko [a], Victoria Vilchez [a], Oriol Gavalda-Diaz [a,b], Florian Bouville [a], Eduardo Saiz [a,*]

[a] Centre of Advanced Structural Ceramics, Department of Materials, Imperial College London, London SW7 2AZ, United Kingdom
[b] Composites Research Group, University of Nottingham, Nottingham NG7 2RD, United Kingdom

ARTICLE INFO

Keywords:
Additive manufacturing
Ceramics
Interlayers
Mechanical properties
Toughness

ABSTRACT

The additive manufacturing of ceramic composites with tailored microstructures is still challenging and time-consuming. However, there is great interest as it may enable the implementation of novel materials architectures following computer designs. In this work, we demonstrate a straightforward method to obtain ceramics with a network of continuous weak interlayers designed to increase fracture resistance using alumina as a model system. This is achieved by combining direct ink writing with the coextrusion of multi-material pastes with carefully matched rheology based on thermally reversible hydrogels and inorganic powders. The printed Al_2O_3 bars with and without weak interlayers exhibit strengths ranging between 180 and 360 MPa and K_{IC} ~ 3 MPa•$m^{1/2}$. The introduction of weak interlayers using different raster patterns, such as length wise and Bouligand alignments can be used to direct crack propagation and promote gradual failure. The result is an improvement in the fracture energy up to 230 J/m^2 and K_J up to 9 MPa·$m^{1/2}$. These results suggest the potential of manufacturing ceramics with enhanced mechanical properties by using robocasting with multi-material inks to engineer complex interlayer networks.

1. Introduction

The advent of additive manufacturing (also called 3D printing) has facilitated the fabrication of materials with complex be-spoken shapes without the use of molds. The term encompasses a suite of technologies, including robocasting, selective laser sintering, digital light processing, etc. that build parts layer-by-layer according to CAD models [1]. They have been applied to metals, polymers, and ceramics [2–5]. Compared to more conventional processing techniques, additive manufacturing is attractive and sustainable as it can minimize the amount of material and post processing operations (e.g., machining) required. A less explored area is the use of additive manufacturing to manipulate the materials structure at the nano to micro-scale in order to optimize performance.

Additive manufacturing of ceramics is appealing as they are widely used in structural and functional applications due to their strength, high temperature stability, oxidation resistance, and biocompatibility [6–9]. However, their main drawback is their intrinsic brittleness, which limits their implementation in structural applications. Different strategies have been investigated to overcome this problem and improve their toughness, like designing specific microstructures and introducing reinforcements [10]. For example, carbon or silicon carbide fibers are used as reinforcements in ceramic matrix composites to promote crack deflection, fiber bridging and pull-out [11,12]. Multilayered composites alternating weak and strong layers have also been prepared (typically the layers are flat and prepared by tape casting). These materials exhibit diverse toughening mechanisms at room and elevated temperatures [13–16]. Other materials use microstructural designs inspired by toughening mechanisms found in natural materials. For instance, synthetic nacre-like structures, in which inorganic lamellar structures are oriented in a compliant matrix, have been fabricated by 3D printing. This nacre-like architecture enhances toughness by crack deflection around rigid lamellae and bridging [17]. The toughness can also be improved in ceramics composites with Bouligand structures, where helicoidal alignment of fibers or platelets in a weak matrix contributes to crack twisting, branching, delamination and promotes isotropic response to in-plane loading [18–20]. In all these materials, the toughening mechanisms rely on the engineering of interfaces to generate a tortuous crack path and absorb more energy during fracture [17,18,

* Corresponding authors.
E-mail addresses: s.zhou18@imperial.ac.uk (S. Zhou), e.saiz@imperial.ac.uk (E. Saiz).

https://doi.org/10.1016/j.actamat.2023.118704
Received 14 September 2022; Received in revised form 9 January 2023; Accepted 12 January 2023
Available online 1 February 2023

21–24].

Paste coextrusion using filaments with core-shell structures is an alternative approach to fabricate multi-material composites through a single printing step. Recent works have focused on the combination of a brittle shell and a tough or hollow core [4,25–29]. Printing systems for coextrusion usually consist of a modified coaxial printhead equipped with multiple feedstock materials. In some cases, the printhead has a block in the center to form hollow filaments. Carbon-ceramic and hollow ceramic filaments with core-shell structures were extruded from modified coaxial printheads [4,26,30,31] and the mechanical performance of the printed scaffolds was improved when polymer was impregnated in the hollow core [31]. Toughening has been observed in polymer systems by introducing a compliant interfacial layer [25]. Multi-material composites were also prepared by formulating ink cartridges with core-shell structures [3,27,29]. After assembling cylindrical core and shell cartridges in a single cartridge as feed rod, the filaments were pushed through a nozzle tip. By adjusting the rheology, the filaments retained the coaxial structure of the cartridge. Ceramics reinforced with a compliant metal, Nickel, or short carbon fibers were coextruded in this way to fabricate composites with elevated mechanical performance through crack deflection and fiber bridging [3,32]. The above coextrusion methods have been mostly applied on hollow ceramic scaffolds, polymer-polymer lattices and polymer-ceramic scaffolds with only a few reports on ceramic dense parts [32].

Here, we propose a method to engineer a network of weak interlayers in ceramic bodies by extruding filaments with a core shell structure and a porous interfacial layer between core and shell. The goal is to design a network of interlayers that will direct crack propagation to improve fracture resistance. To achieve this, we have formulated pastes based on ceramic hydrogels and assembled these pastes in a core-shell structure. To allow different pastes to be coextruded, their rheological behavior needs to be carefully matched. Alumina was used for both, core and shell material, and the interlayer was composed of a mixture of Al_2O_3 and graphite with different volume ratios. The graphite flakes with high aspect ratio burn out during sintering leaving a weak porous layer with plate-shaped pores aligned tangentially to the core. We link structural characterization and mechanical testing to analyze the effect of this network of interlayers on the mechanical properties.

2. Experimental

30wt% Pluronic F127® gel was prepared by mixing Pluronic F127 powder (Sigma-Aldrich, UK) and deionized water with a weight ratio of 3:7. This mixture was stored in the fridge for 24 h to form a homogenous and clear gel. Al_2O_3 powder (SMA6, d_{50}=0.2μm, Specific Surface Area 7m^2/g, Baikowski, France) was sieved using a plastic 100 μm sieve to break agglomerates and graphite powder (APS 7–11 μm, 99%, Alfa Aesar, UK) was used as received. For the preparation of the core and shell paste, 37vol% Al_2O_3 powder was added to Pluronic F127 gel along with 1wt% Dolapix CA (to the weight of the powder). It was then mixed in a Thinky ARE-250 planetary mixer at 2000 rpm for 2 min, repeatedly for 3–5 times until a smooth paste without visible powder agglomerates was obtained. The mixing container was placed in iced water to cool between each mixing. A final defoaming step at 2200 rpm for 10 min was used to remove air bubbles trapped in the paste. Likewise, the paste for the interlayers was prepared by replacing Al_2O_3 powder with a

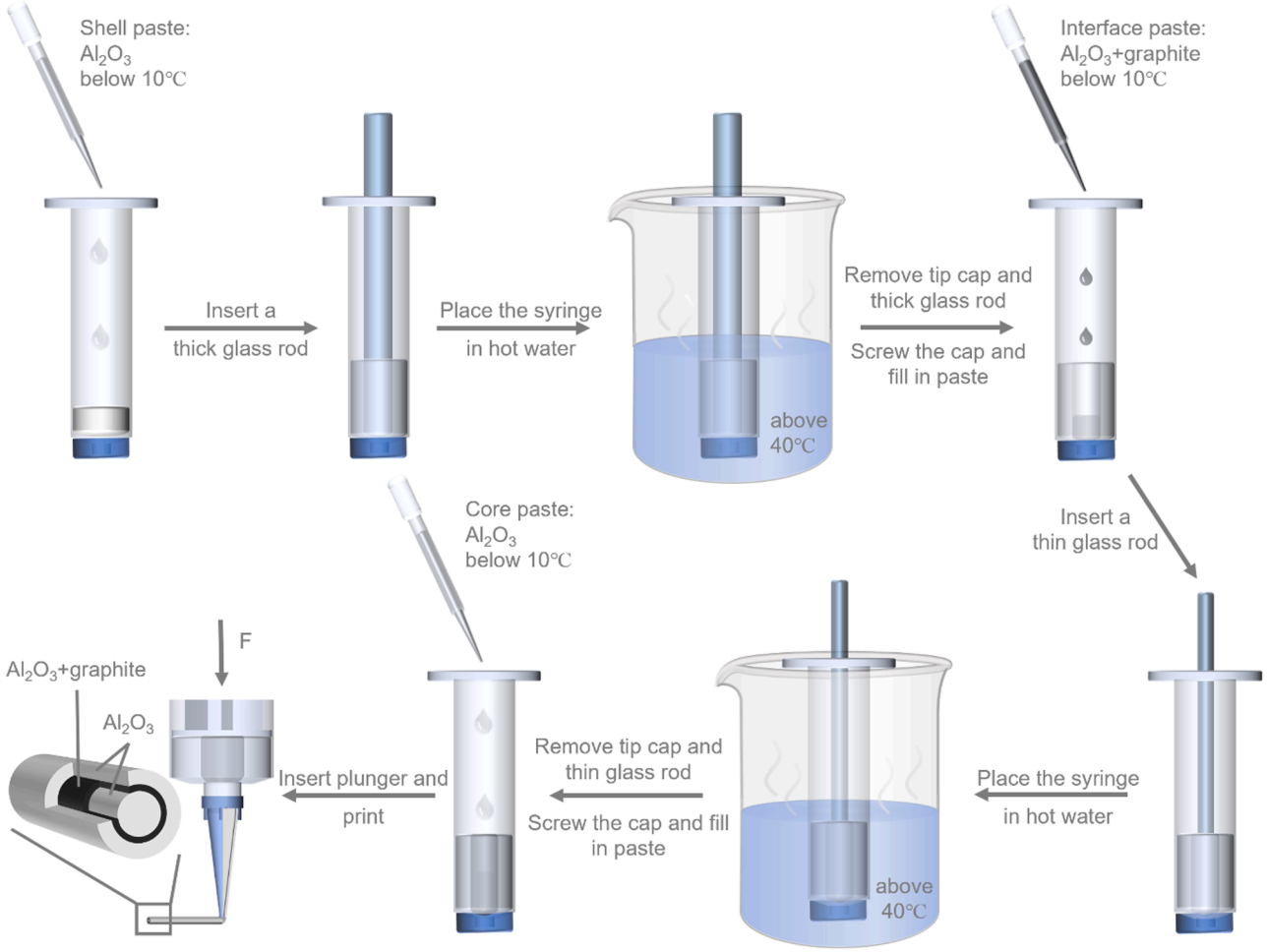

Fig. 1. Schematic showing the steps used to prepare a printing cartridge with a core shell structure.

mixture of Al_2O_3 and graphite in the volume ratio of 5:5 or 4:6, denoted as $(Al_2O_3)_{0.5}C_{0.5}$ and $(Al_2O_3)_{0.4}C_{0.6}$, and was homogenized in the same manner as the core and shell paste.

Shell, interlayer and core pastes were cooled down below 10 °C and sequentially transferred into a 10 mL syringe with a tip cap as depicted in Fig. 1a. A thick glass rod (8 mm in diameter) coated with vacuum grease was inserted after the liquid-like shell paste was casted in a 10 mL syringe with an inner diameter of 15.78 mm. This syringe was then sealed with a cap at the tip and placed in hot water over 40 °C to form a gel able to maintain its shape. With the purpose of balancing the pressure and preventing deformation of the existing shell structure, the tip cap was unscrewed before the glass rod was taken out. The same procedure was repeated twice to transfer the interlayer paste containing Al_2O_3 and graphite powder and the core paste in turn. A thin glass rod with a diameter of 4 mm was inserted to shape the interlayer and make space for the core paste. Finally, the plunger of the syringe was notched at the edge with a scalpel and inserted into syringe to expel the air from the interior and prevent the ink from drying. By applying force on the plunger and matching the rheological behavior of each paste, filaments with the core shell structure were extruded through a conical tip.

Printed parts include single filaments, grids and bars (30 × 4 × 5 mm^3) fabricated using different raster patterns. Single filaments and bars are used to measure mechanical properties and the grid structure facilitates the observation of the microstructure and the structural consistency of the extruded filaments with the core-shell structure. Two kinds of core-shell cartridges with different Al_2O_3/graphite ratios (50/50 and 40/60 in volume) in the interlayer layer were used. For comparison, Al_2O_3 bars with the same dimensions and without interlayer were also printed. Printing was carried out on a 3dInks direct ink writing system (USA) using a conical nozzle with an inner diameter of 0.41 mm. The core shell paste was extruded at a printing speed of 6 mm/s on a Teflon substrate greased with oleomargarine. To fabricate dense ceramic parts, the z-spacing (height step) was set as the filament diameter divided by 1.2 [33]. Bars with two raster patterns (length wise and Bouligand with a pitch angle γ of 30°) were printed as shown in Fig. 2. Al_2O_3 and $Al_2O_3/(Al_2O_3)_{0.5}C_{0.5}/Al_2O_3$ core-shell filaments (denoted as AC50) were printed in the length wise pattern and $Al_2O_3/(Al_2O_3)_{0.4}C_{0.6}/Al_2O_3$ core-shell materials (denoted as AC60) were built using both patterns. The printed parts were placed in an oven with a humidity of 72±3% at 30 °C for 2 days until completely dried and cold isostatically pressed at 300 MPa for 5 min. Subsequently, they were heated in air at 1 °C/min to 350 °C, after 1 h at this temperature they were heated at 2 °C/min to 500 °C and held for 2 h to burn out the Pluronic. They were sintered at 1550 °C for one hour in air with a heating rate of 5 °C/min.

The rheological behavior of each paste was determined using a TA Instruments Discovery HR-1 rheometer with a 40 mm parallel plate geometry and a 1000 μm gap. Few droplets of distilled water were added in the solvent trap to prevent water evaporation. Flow ramp measurements with shear rate varying from 0.01 s^{-1} to 100 s^{-1} and oscillatory tests at an oscillation stress from 1 to 2000 Pa at 1 Hz were performed to evaluate the rheological behavior of the pastes at 25°C.

The density and porosity were measured using the Archimedes method at room temperature. The microstructure of the fracture surfaces and polished parts was observed with JEOL 6010 SEM with an acceleration voltage of 20 kV, a thin gold film coating on the surface was used to improve electrical conductivity. The dimensions of the core, interlayer and shell in each filament were measured with Image J software analysis of the SEM images. Each filament was measured with two orthogonal straight lines across the center and more than 40 filaments from different syringes were examined for each composition. In order to determine the porosity of the interlayers, samples infiltrated with epoxy were polished down to diamond 1 μm. The interlayers were observed in SEM with backscattered electrons and image analysis (Image J) was used to quantify the porosity (Fig. S1).

The tensile surfaces of ten sintered bars (25 × 2.8 × 2.8 mm^3) of each composition and raster pattern were polished down to diamond 1 μm and their edges beveled prior to performing three-point bending tests. A notch was cut in three bars of each composition and raster pattern in the above dimension with a 0.25 mm diamond wafering blade and then sharpened with a razor blade and 1 μm diamond suspension in order to prepare Single-Edge Notched Beam (SENB) specimens for the measurement of toughness. The same number of SENB specimens with a dimension of and 25 × 3 × 6 mm^3 was also prepared. A span, S, of 15 mm and a displacement rate of 0.1 mm/min were used. Bending was carried out in a Zwick iLine universal testing machine. To measure displacement accurately during the three-point bending tests of SENB specimens, a high-resolution camera was used to capture the real displacement. One image per second was taken while testing and imaging was synchronized with the force-displacement curves. These images also allowed us to monitor the crack extension Δa on the surface and plot the R-curve according to ASTM E1820. The maximum valid crack extension is defined as $\Delta a_{max}=0.25b_0$, where b_0 is the initial uncracked ligament width. Nonlinear elastic fracture mechanics was considered, where the nonlinear strain-energy release rate J includes the elastic contribution J_{el} and plastic contribution J_{pl}. The elastic one J_{el} is given by:

$$J_{el} = K_i^2/E' \tag{1}$$

where E' is $E/(1-\upsilon^2)$, E is the Young's modulus, υ is Poisson's ratio and K_i is the fracture toughness at a given crack length a_i:

$$K_i = \frac{F_i S}{(BW^{3/2})} f\left(\frac{a_i}{W}\right) \tag{2}$$

where S is the supporting span, B is the bar thickness and W is the width, a_i is the crack length and $f\left(\frac{a_i}{W}\right)$ is:

$$f\left(\frac{a_i}{W}\right) = \frac{3\left(\frac{a_i}{W}\right)^{1/2}\left[1.99 - \frac{a_i}{W}\times\left(1-\frac{a_i}{W}\right)\left(2.15 - 3.93\frac{a_i}{W} + 2.7\left(\frac{a_i}{W}\right)^2\right)\right]}{2\left(1+2\frac{a_i}{W}\right)\left(1-\frac{a_i}{W}\right)^{3/2}} \tag{3}$$

The plastic contribution J_{pl} is calculated using four different methods based on the ASTM E1820 standard. For method 1, it is expressed as:

$$J_{pl} = \frac{1.9A_{pl}}{Bb} \tag{4}$$

where A_{pl} is the plastic area under the force-displacement curve and it is calculated by subtracting from the total area the elastic component (assuming there is no change in compliance), b is the uncracked ligament width. The J integral values for method 1 are corrected using the following expression:

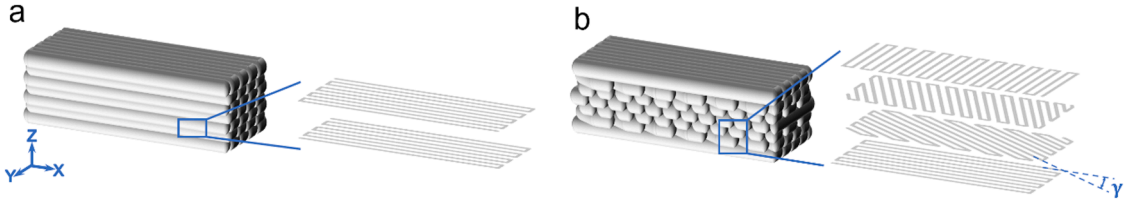

Fig. 2. Schematic of printed bars with two raster patterns (a) length wise alignment (b) Bouligand structure (the pitch angle is γ).

$$J = J_{el} + \frac{J_{pl}}{1 + \left(\frac{\alpha - 0.5}{\alpha + 0.5}\right)\frac{\Delta a}{b}} \tag{5}$$

where α is 1 for SENB specimen. The J_{pl} in method 2 is calculated iteratively using the following expression:

$$J_{pl(i)} = \left[J_{pl(i-1)} + \frac{1.9\left(A_{pl(i)} - A_{pl(i-1)}\right)}{b_{i-1}B}\right] \times \left[1 - \frac{0.9 \times (a_i - a_{i-1})}{b_{i-1}}\right] \tag{6}$$

Here, A_{pl} is measured the same as method 1. Method 3 takes the compliance into account. The A_{pl} is calculated from:

$$A_{pl(i)} = A_{pl(i-1)} + (F_i + F_{i-1})\frac{v_{pl(i)} - v_{pl(i-1)}}{2} \tag{7}$$

where $v_{pl(i)}$ is the plastic part of the force-displacement given by $v_{(i)} - F_i C_i$, $v_{(i)}$ is the displacement and C_i is determined from:

$$C_i = \frac{1}{EB}\left(\frac{S}{W - a_i}\right)^2 \times \left[1.193 - 1.98\frac{a_i}{W} + 4.478\left(\frac{a_i}{W}\right)^2 - 4.443\left(\frac{a_i}{W}\right)^3 + 1.739\left(\frac{a_i}{W}\right)^4\right] \tag{8}$$

In the case of method 4, J is given by $1.9A_{tot}/Bb$, where A_{tot} is the total area under the force-displacement curve [22]. The stress intensity K_J is then calculated directly as $\sqrt{JE}$.

In-situ three-point bending tests in a Zeiss Sigma FEG-SEM were conducted on a 300 N Tensile Tester (DEBEN, UK) with a span of 21 mm and a displacement rate of 0.1 mm/min to observe crack propagation and determine the strength of single filaments. Due to the anisotropy of Bouligand structures, they were tested in two directions (perpendicular and parallel to the printing plane). The 3D profile and roughness of the fracture surfaces were measured by 3D digital optical microscopy (VHX-900F, Keyence, Germany) and 3D optical interferometer (NewView 200, Zygo, USA).

3. Results

3.1. Core-shell structure ink preparation and printing

All pastes are based on Pluronic gels with inorganic powders. Pluronic F-127 is a polyethylene oxide-poly propylene oxide hydrogel that has reversible gelation upon heating at ~15 °C for a 30wt% Pluronic gel (Fig. 3). The temperature-sensitive nature of this gel is a prerequisite for preparing ink cartridges with a core shell structure. When the temperature rises from zero to room temperature, a liquid-gel transition occurs. The 30wt% Pluronic suspension behaves like a liquid below 10 °C and it becomes a gel above 20 °C. The addition of ceramic powder results in an increase in viscosity around one order of magnitude. The transition temperature is similar for gels with and without ceramic loading. This increase of viscosity with temperature and increasing inorganic content is attributed to a high concentration of micelles and a percolating network of inorganic powders. The fluidity of the pastes below 10 °C allows easy transfer of the paste into the syringe and helps to avoid air trapping. Therefore, the component pastes were cooled below 10 °C in iced water, to prepare the pastes with core-shell structure.

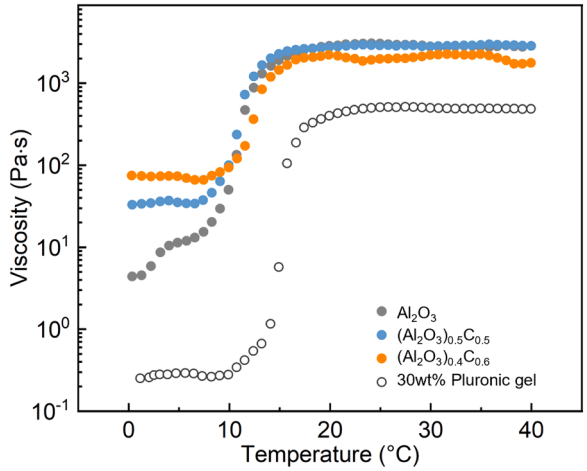

Fig. 3. Viscosity-temperature curve of 30wt% Pluronic gel with inorganic powders.

3.2. Rheology for paste co-extrusion and microstructure of the samples

The pastes for robocasting should be extruded through a narrow nozzle, and the filaments should hold their shapes. This requires the paste to be shear thinning. The behavior of the shear thinning pastes in this work can be described using the Herschel-Bulkley equation: [34]

$$\tau = \tau_y + K\dot{\gamma}^n \tag{9}$$

where τ is the shear stress, τ_y is the yield stress, $\dot{\gamma}$ is the shear rate, K is the viscosity parameter and n is the shear thinning coefficient ($0<n<1$).

In the flow ramp measurements (Fig. 4a), the viscosity η decreases exponentially with the rise of the shear rate, confirming the shear thinning behavior and following a power law

$\eta = K\dot{\gamma}^{n-1}$. From this viscosity curve, the value of viscosity parameter K and shear thinning coefficient n can be calculated by fitting the data at intermediate shear rates, where the pastes are in steady state and no slippage occurs. All pastes display similar n ~0.2 and K ~4000 Pa·s^n.

The viscoelastic properties like equilibrium storage modulus G'_{eq} and flow point, regarded as the yield stress τ_y in this work, are determined in the oscillatory tests (Fig. 4b). At the beginning of the test, the stress is low and the storage modulus G' is higher than the loss modulus G''. The paste is within the linear viscoelastic region with a constant storage modulus G'_{eq} When the stress is above 300 Pa, G' drops whereas G'' gradually increases. The paste starts to deform plastically, internal friction generates thermal energy [36] and the flow point (the crossover point of G' and G'') represents the transition of gel from solid-like to liquid-like (Fig. 5a) [33,37]. The rheological properties of all pastes are summarized in Table 1.

Polished cross-sections of sintered grids with a core shell structure after sintering are presented in Fig. 5b. Although core and shell are not perfectly concentric in the filaments (Fig. 5b) a continuously porous Al_2O_3 interlayer is present between both. The single filament diameter in both grids is ~280 μm. The radius of the core and the thickness of interlayer are ~35 μm and the thickness of the shell is ~70 μm (Fig. 5c). The ratio of core radius, thickness of interlayer and shell of sintered parts is 1:1:2, which corresponds to the diameter ratio of the syringe, the thick and thin glass rod used for preparing the core-shell cartridge. This ratio indicates an appropriate match of the rheological parameters of the component pastes.

The linear shrinkage of bars in length and width during drying is 10.0±1.0%. After CIP and sintering, the total shrinkage from just printed to sintered is 30.3±0.5%. The porosity of all bars is below 4%, with the lowest porosity of 1.3% in the pure alumina bars. It is worth noting that in order to obtain dense materials, the vertical printing distance between each filament was set as $d/1.2$ (where d is the inner diameter of the nozzle) to eliminate printing gaps in final products. The approach was successful, as shown in the polished cross sections (Fig. 6). However, this printing distance leads to the deformation of the filaments (Fig. 6b–d). The cores exhibit periodic droplet-shaped cross sections in the length wise alignment and various degrees of deformation are observed in the Bouligand structure due to the fact that a straight cut can never be perpendicular to all the cores (Fig. 6d).

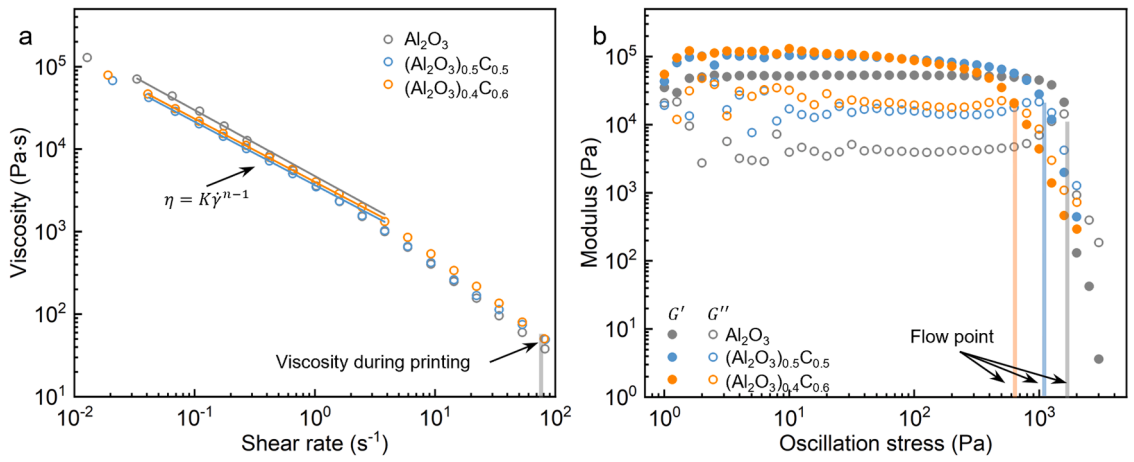

Fig. 4. Rheological behavior of different pastes at 25 °C (a) Viscosity curves. The viscosity of the paste in the nozzle during printing is estimated using the method described in reference [35] (b) Determining the flow point from the oscillatory test.

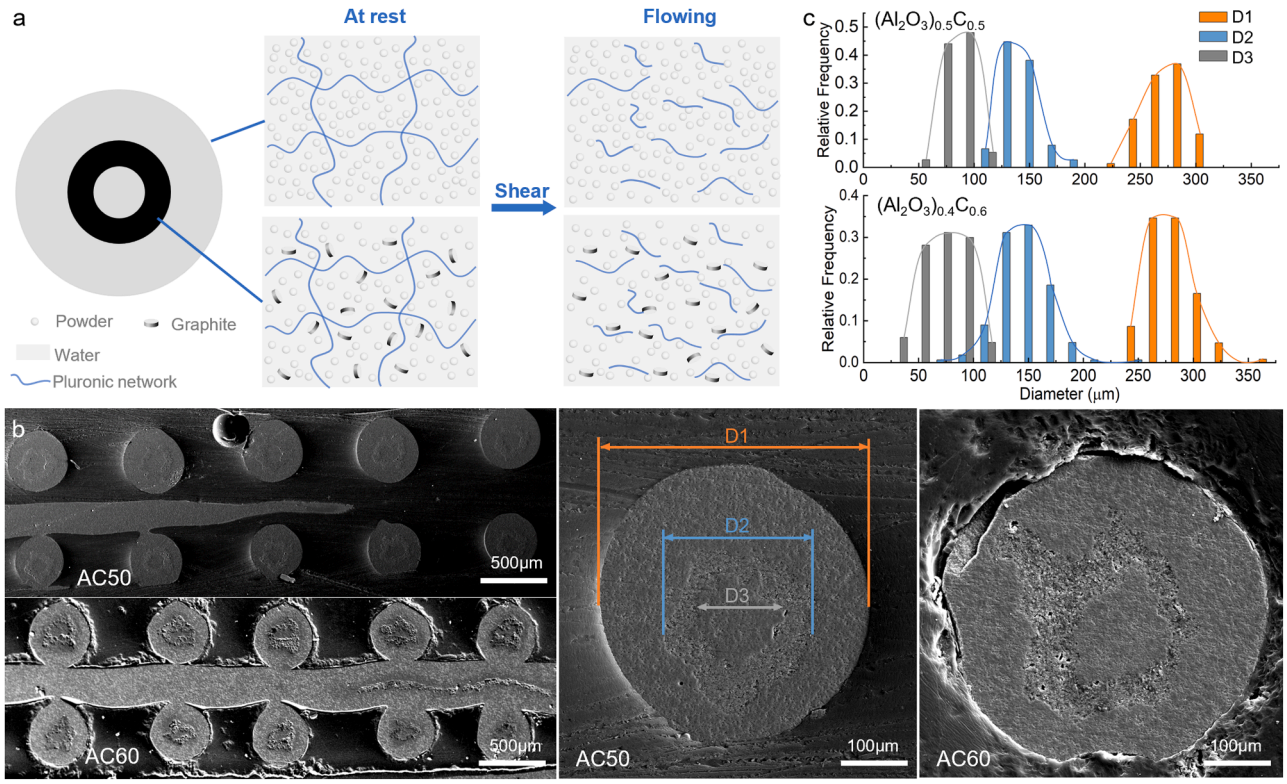

Fig. 5. (a) Illustration of the core shell structure in gel state and flowing state (b) Microstructure of sintered AC50 and AC60 grids (c) Distribution of the core, interlayer and shell dimension in single filaments. T.

Table 1
Rheological properties of all pastes at 25 °C.

Paste	Viscosity during printing (Pa·s)	Shear thinning coefficient η	Viscosity parameter $K(Pa{\cdot}s^n)$ K ($Pa{\cdot}s^n$)	Equilibrium storage modulus G'_{eq} (Pa)	Flow point τ_y (Pa)
Al_2O_3	56±14	0.19±0.04	5228±680	5.1×10^4	1648
$(Al_2O_3)_{0.5}C_{0.5}$	60±11	0.22±0.01	4056±542	9.5×10^4	1129
$(Al_2O_3)_{0.4}C_{0.6}$	53±1	0.25±0.02	4034±24	1.2×10^5	642

3.3. Mechanical properties

The mechanical properties of the bars are summarized in Table 2. Bars with Bouligand alignment were tested in two directions, denoted as Bouligand T and Bouligand S in Fig. 7a with the tensile surface in orange. The samples printed with 14 layers were polished in all sides, therefore the orientation of the filaments in the tensile layer may vary for Bouligand S (at 0, 30, 60 or 90°). Filament orientation will not vary for the length wise and Bouligand T configurations. This variability is partially reflected in the statistical scatter of the data. Regardless of the interlayer, all single filaments present a similar strength of ~600 MPa (Fig. S2). For bars, the value of flexural strength σ_f decreases when adding interlayers from 360 MPa without weak interlayers to 180 MPa

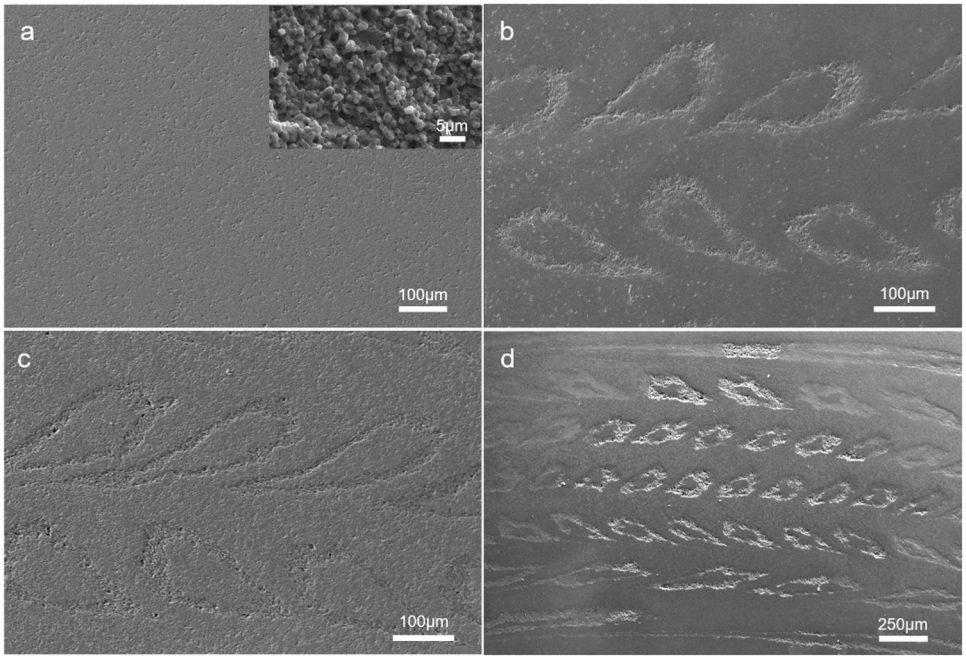

Fig. 6. Polished fracture surface of robocasted Al_2O_3 without and with core-shell structure weak interlayer (a) pure Al_2O_3, the insert shows a fracture surface, printed length wise (b) AC50, printed length wise (c) AC60, printed length wise, (d) AC60, printed with Bouligand alignment.

Table 2
Density and mechanical properties of 25 × 2.8 × 2.8mm^3 Al_2O_3 bars with and without the continuous weak interlayer.

Sample	ρ_{real} (g/cm^3)	Relative density (th%)	σ_f (MPa)	K_{IC} (MPa·m$^{1/2}$)	$K_{J,\ limit}$ (MPa·m$^{1/2}$)	Work of fracture (J/m^2)
Al_2O_3	3.91±0.03	98.7±0.8	357±38	3.4±0.4	–	–
AC50, length wise	3.84±0.03	97.0±0.7	319±64	3.2±0.4	–	–
AC60, length wise	3.83±0.03	96.7±0.7	221±45	3.1±0.4	9.4±2.7	230±57
AC60, Bouligand T			181±45	2.8±0.5	–	68±19
AC60, Bouligand S			183±41	2.9±0.8	7.7±0.8	102±46

with the interlayers. Moreover, all unnotched samples containing porous interlayers are not completely broken after the load drops, suggesting a higher toughness.

Calculated using the force at which the force-displacement curve stops being linear in Eq. (2), the K_{IC} for all samples is ~3 MPa·m$^{1/2}$. Fracture is always intergranular (Fig. 6a insert) regardless of the differences in microstructures and raster patterns. In the force-displacement curves of SENB samples (Fig. 7b), the dense Al_2O_3 and AC50 bars exhibit a linear elastic response and brittle fracture behavior, like typical ceramics. The latter show a very small amount of crack deflection (Fig. 7d). Interestingly, by using more porous interlayers and altering the raster patterns, AC60 bars in length wise and Bouligand alignments fail in a more gradual fashion. The R-curves of a representative bar, AC60 in length wise calculated with different methods (Fig. 7h) exhibit similar rising trends. Depending on the method, the maximum K_J of AC60 bars in length wise ranges between 9.4 and 14.3 MPa·m$^{1/2}$. Method 3 is more conservative as it considers the evolution of both J_{el} and J_{pl} with each increment of crack length, and gives a J_{el} of 0.03 kJ/m^2 and $J_{pl,\ limit}$ of 0.23 kJ/m^2 for AC60 bars in length wise orientation. The other methods overestimate the plastic contribution (J_{pl}) at the beginning of crack extension (Fig. S3). For this reason, the toughness given by method 3 is used as a reference and is listed in Table 2, with the corresponding R-curves of all samples in Fig. 7i. Among these samples, bars printed using a length wise alignment exhibit the highest toughness of 9.4 MPa·m$^{1/2}$. Length wise and Bouligand S bars present a rising R-curve that reaches a plateau before the ASTM limit in crack length for a valid measurement. It needs to be noted that the higher K_J values obtained in some of the AC60 bars with length wise alignment (Fig. 7i) arises from cracks branching in two. The crack measurements on these curves are based on the development of the main crack and the corresponding $K_{J,\ limit}$ (the maximum value) is regarded as the point before a secondary crack develops. This secondary crack may initiate inside the bar and it is only observed when it propagates to the surface resulting in an overestimated $K_{J,\ limit}$. Moreover, the R-curves of larger and smaller samples are slightly different, indicating that the measured toughness might be affected by sample size although both of them exhibit similar crack paths (Fig. S4). The work of fracture measured for the large samples doubles the one measured in the small samples, regardless of their raster patterns. The $K_{J,\ limit}$ increases from 9.4 MPa·m$^{1/2}$ in small AC60 bars length wise (2.8 × 2.8mm^2 in cross-section) to 16.1 MPa·m$^{1/2}$ in big ones (3 × 6mm^2 in cross-section).

3.4. Crack-growth observations

Crack propagation was monitored *in-situ* during three-point bending tests of SENB samples in the SEM. The observations were compared with images of the corresponding fracture surfaces. As observed in Fig. 7e and g, the weak interlayers promote a tortuous crack path that results in uneven fracture surfaces. The fracture surfaces of different raster structures are apparently different, and their extrinsic toughening mechanisms are discussed in detail below.

Extrinsic toughening stems from the periodical core-shell architecture and the contribution of the weak interlayers. AC60 bars in the length wise configuration (Fig. 8) are basically toughened by crack deflection. Pull out or bridging is also observed (Fig. 7e), which is the presumable reason for a higher toughness in the longitudinal direction.

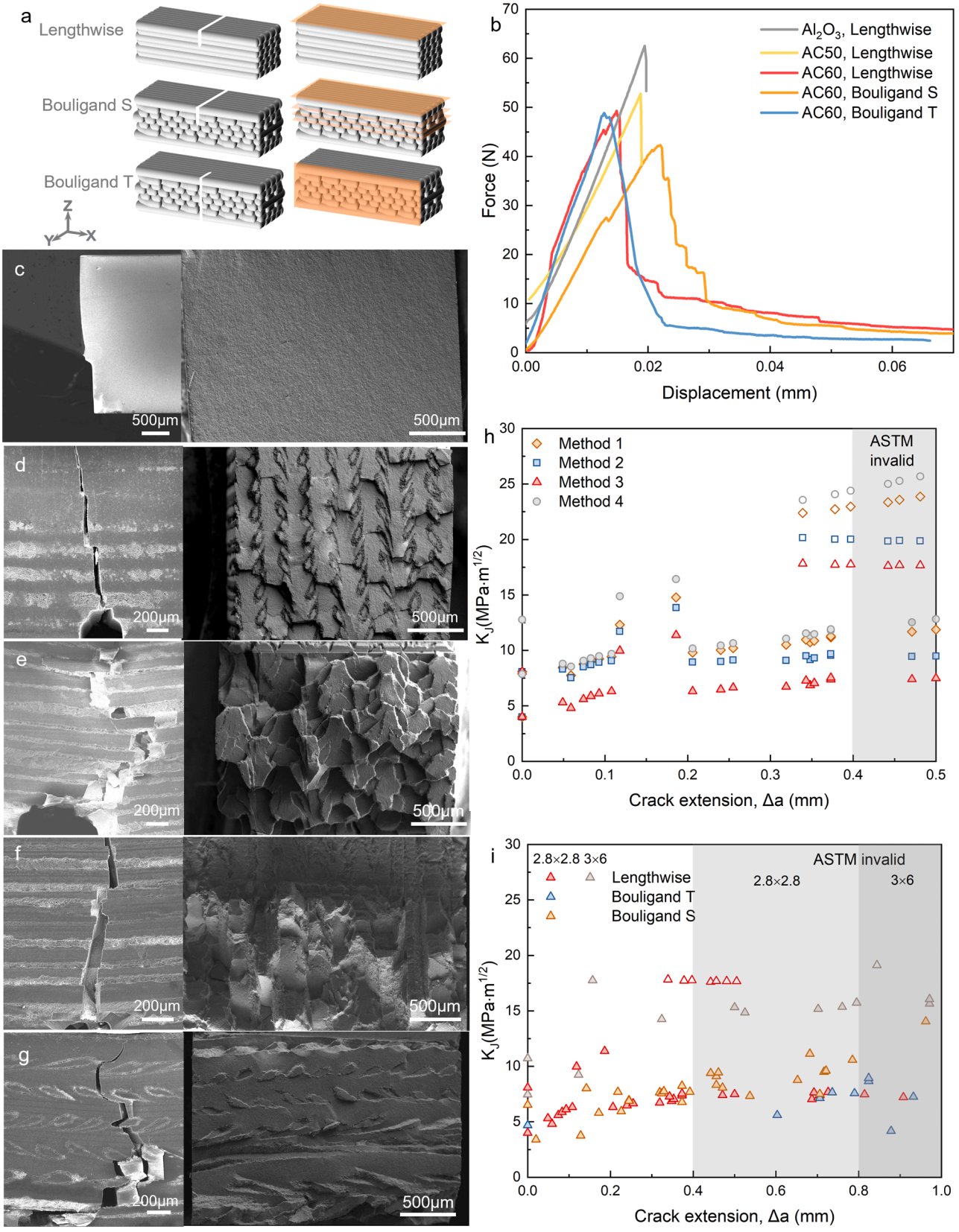

Fig. 7. Fracture behavior of SENB samples. (a)Schematic of samples with different raster patterns (b) Force-displacement curves of SENB samples with similar dimension 25 × 2.8 × 2.8 mm^3. Representative crack paths and the corresponding fracture surfaces of (c) Al_2O_3, length wise (d) AC50, length wise (e) AC60, length wise (f) AC60, Bouligand T alignment (g) AC60, Bouligand S alignment. (h) Comparison of R-curves of AC60 bars, length wise with a 2.8 × 2.8 mm^2 cross-section calculated with different methods, shadowed area marks the ASTM invalid area for a valid measurement. Open symbols mean the developing of a secondary crack. (i) R-curve of AC60 bars, with the ASTM limits of bars with a 2.8 × 2.8 and 3 × 6 mm^2 cross-section marked by the shadowed area.

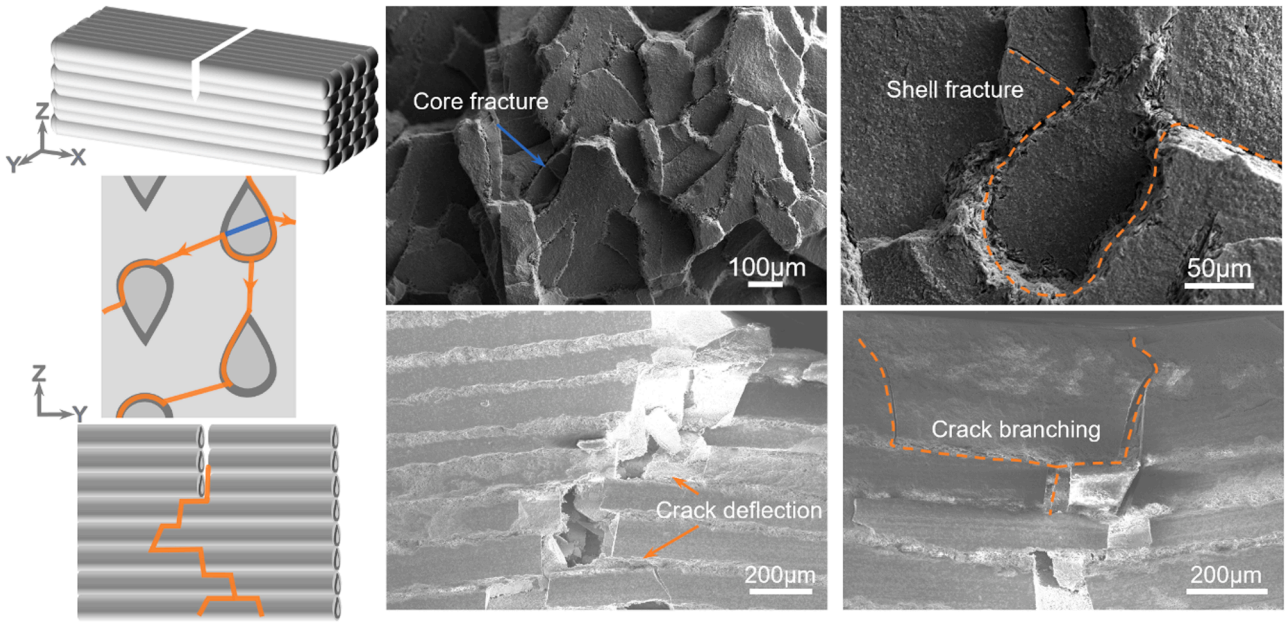

Fig. 8. Toughening mechanisms in AC60 length wise showing how crack deflection happens in the longitudinal directions, parallel to the weak interfaces.

The interlayers are weak enough to deviate and arrest the crack until the core breakage. It functions like a mixture of thin laminate and fiber reinforced composites (with the core acting as a fiber). The interlayer in AC60 bars with Bouligand T doesn't work as effectively as in the length wise arrangement because interlayers perpendicular to the notch make the crack deflect 90° and the others deflect it in a smaller degree (Fig. 9). The Bouligand S structure can be regarded as helicoidal, composed of multiple layers with a pitch angle and weak interlayers to enhance toughness. The filaments at individual layers ahead of the crack tip align in the same direction. Crack twisting with an angle of ~12° occurs at the crack tip (Fig. 10). This provides an effective mode mixity locally and consumes more energy. Crack deflection along the contour of a weak interlayer between adjacent layers can be observed. Crack twisting and deflection harness the advantage of numerous weak interlayers and increase energy absorption during fracture. Therefore, a progressive failure is observed in the bending tests.

4. Discussion

4.1. Microstructure

Multi-material coextrusion provides a novel method to form core-shell filaments, with a particular interlayer between core and shell. This interface can be designed with a controlled microstructure to effectively promote crack deflection. The fact that core and shell are not perfectly concentric (Fig. 5b) can be due to the manual preparation of the cartridges. When the glass rod is pulled out, a small amount of the previously casted paste sticks to it. This causes the irregular shape of each layer. In addition, a thick or thin glass rod not placed in the center of the syringe leads to a not perfectly symmetric geometry. The method employed to determine the dimensions of core, shell and interlayer using two orthogonal straight lines across the center of the filament, combined with the irregular shape and asymmetric geometry results in the

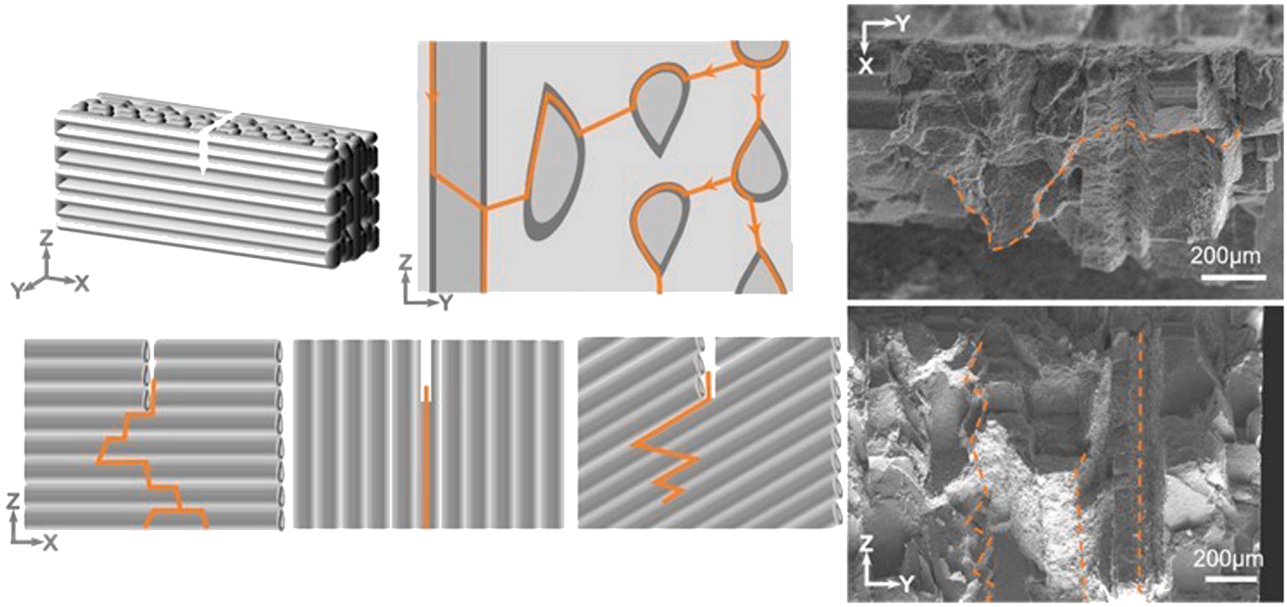

Fig. 9. Toughening mechanisms in AC60 Bouligand T where interlayers in different layers along Y direction react differently.

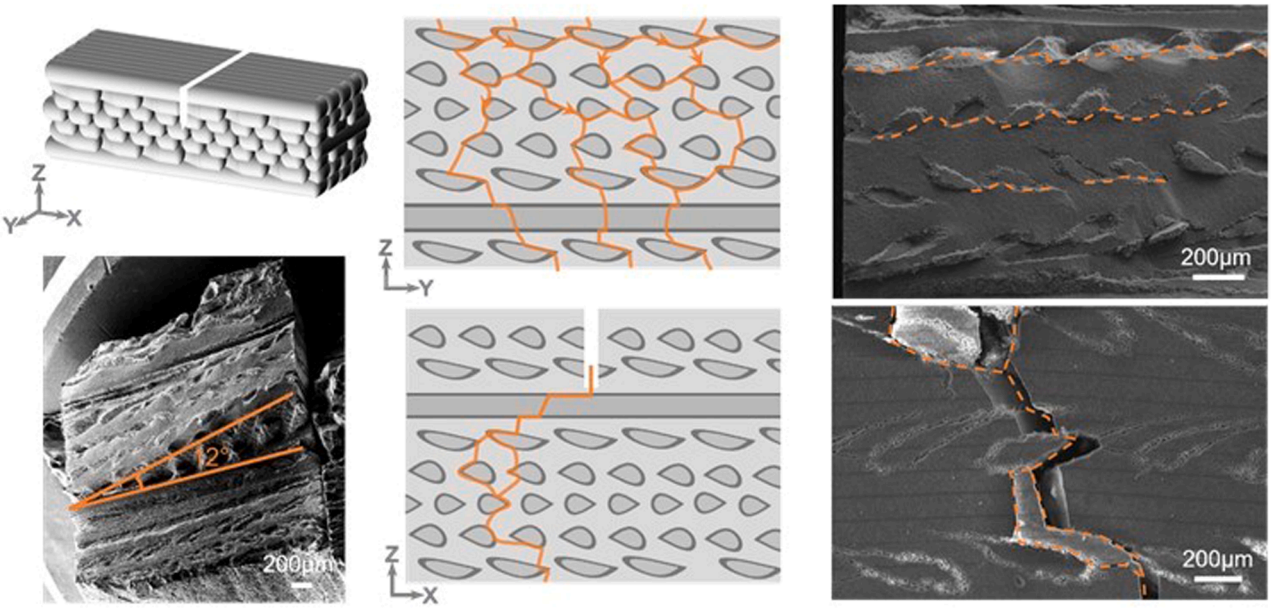

Fig. 10. Toughening mechanisms in AC60 Bouligand S, presenting both crack deflection and twisting.

observed scattering of the values (Fig. 5c). Another reason is related to the rheology of different pastes. Although similar viscosity during printing (~60 Pa·s), shear thinning coefficient (~0.2) and viscosity parameter (~4000 Pa·s^n) among all pastes ensure continuous co-extrusion, the yield stress, which decreases with the addition of graphite powder, is not comparable.

Proper coextrusion requires different pastes with similar viscoelastic responses, especially the yield stress τ_y, shear thinning coefficient n and viscosity parameter K, so as to allow the generation of comparable velocity profiles within the nozzle. Using a cylindrical printing nozzle for comparison, the velocity V profile of a Herschel-Bulkely fluids as a function of the distance from the cylinder central axis (r) can be described by the following constitutive equations: [38]

$$r \le r_p \qquad V_p = \left(\frac{1}{K}\right)^{1/n} \frac{R}{\tau_w} \frac{n}{n+1} \left(\tau_w - \tau_y\right)^{(1+n)/n} \tag{10}$$

$$r_p \le r \le R \qquad V = \left(\frac{1}{K}\right)^{1/n} \frac{R}{\tau_w} \frac{n}{n+1} \left[\left(\tau_w - \tau_y\right)^{(1+n)/n} - \left(\frac{\tau_w}{R} r - \tau_y\right)^{1+n/n}\right] \tag{11}$$

where r_p is the radius of the plug zone ($\frac{R\tau_0}{\tau_w}$), V_p is the velocity of the plug zone, R is the radius of nozzle, τ_w is the shear stress at nozzle wall ($\frac{\Delta PR}{2L}$) ΔP is the pressure drop over the length of the nozzle L. At a position close to the center of the nozzle ($r \le r_p$), the fluid is not yielded and flows at a constant velocity V_p. All pastes exhibit a parabolic profile, with a minimum velocity close to the wall and a constant velocity in the middle (Fig. 11a). This velocity profile results in a high velocity gradient ($\frac{dV}{dr} = \left(\frac{1}{K}\right)^{1/n}\left[\left(\frac{\tau_w}{R} r - \tau_y\right)^{1/n}\right]$) around the nozzle wall, up to 250s^{-1}, and gradually decreases toward the center of the nozzle. Although this calculation may suggest that the interlayer is in the plug region, since the printing nozzle is actually conical instead of cylindrical and the determination of n and K could include some errors (the points at low shear rate are not considered), the velocity profiles may vary. The alignment of the graphite flakes with the flow suggests that the interlayer paste may be subjected to a velocity gradient, which could rotate the graphite flakes towards the tangential direction. As such, flake-shaped pores aligning parallel to the flow are retained in the sintered samples inks (Fig. 11b). This alignment of platelets with high aspect ratio was also found in robocasted Al_2O_3 platelets for the same reason [20].

4.2. Mechanical behaviour

As expected, there is a trade-off between strength and toughness with the introduction of weak interlayers using graphite powder as the pore former [39]. The interlayers generate extrinsic toughening mechanisms but the strength of the material decreases due to the presence of weaker

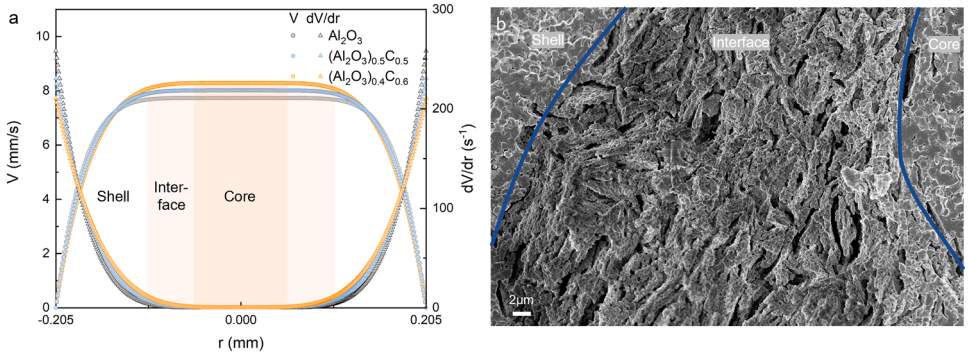

Fig. 11. (a) The velocity profile and its gradient in a 0.41 mm nozzle, the dimension of core, interlayer and shell are labeled (b) Microstructure of fracture surface around a porous alumina interlayer showing high aspect ratio pores that align with the flow of the inks during extrusion.

interlayers containing defects. The SEM images of the fracture surfaces show a grain size of ~2 μm in the dense Al_2O_3 at the core and shell (Fig. 6a). The pores left by the graphite at the interlayer have a flake-like shape with a width of ~10 μm and a thickness of ~0.5 μm comparable to that of the starting graphite powder (Figs. 12 and S5). The effect of defect size on strength of brittle ceramics is described by Griffith/Irwin failure criterion:

$$K_{IC} = Y\sigma_f(\pi a)^{1/2} \tag{12}$$

where Y is a geometric factor (1.77 for defects with a high aspect ratio) [40]. Calculated with the mechanical properties in Table 2, the critical defect size is ~30 μm for Al_2O_3, ~10 μm for AC50 bars, ~20 μm for AC60 bars in length wise and Bouligand structures. As the tensile faces are polished, the calculated defect sizes suggest that failure might generate from the pores at the interlayer left by graphite in the core shell structures. Another source of defects comes from gas bubbles trapped in the filaments or the packing of printing lines (Fig. S6). Particularly, the later can be an issue for bars with Bouligand structure where the calculations suggest a larger critical defect size [20,33]. The poor packing of this structure could allow pores to form between lines during printing and reduce the strength.

The ability of a weak interlayer to deflect the crack is given by the balance between its fracture energy with that of the bulk. There are several models that have shown how the porosity reduces the K_{IC} of ceramics and Eq. (13) has been proposed by Ostrowski et al. for alumina [41]. The fracture energy of the interlayer G^i_{IC} and the bulk G^f_{IC} can be estimated by:

$$K_{IC} = \left(1 - \frac{P}{P_0}\right)^n K_{IC,100} \tag{13}$$

$$E(P) = E_{100}\left(1 - \frac{P}{P_0}\right)^n \tag{14}$$

$$E' = E/\left(1 - \upsilon^2\right) \tag{15}$$

$$G_{IC} = K^2_{IC}/E'(P) \tag{16}$$

where K_{IC} is the initiation toughness, P is the porosity of the interlayer measured by analyzing the SEM images of the polished surface after infiltration with epoxy (Fig. S1), ~15% for the AC50 interlayer and 36% for the AC60 interlayer, $K_{IC,100}$ is the initiation toughness of fully dense samples, E_{100} is the Young's modulus of fully dense Al_2O_3, $E(P)$ is the Young's modulus of porous material, P_0 and n are 0.5 and 1.35 for fine-grained Al_2O_3 with a mean particle size of 0.2 mm, υ is the Poisson's ratio [41]. We can use the calculated fracture energies to estimate if the porous interfaces will be able to deflect the cracks using the He and Hutchinson analysis [42] for the corresponding elastic mismatch α between core and shell. This mismatch can be expressed as:

$$\alpha = \frac{E'_m - E'_f}{E'_m + E'_f} \tag{17}$$

where the subscript m and f are the matrix and fiber in fiber reinforced ceramics. In our core/shell structure, assuming that interlayers are thin, both matrix and fiber are dense Al_2O_3 with the same Young's modulus and Poisson's ratio, so α=0. This corresponds to a critical G^i_{IC}/G^f_{IC} of 0.25 in the He and Hutchinson plot, indicating that lower values will lead to crack deflection along the interface.

Using Eqs. (13)–(16), the calculated G^i_{IC}/G^f_{IC} is 0.64 for AC50 bars and 0.19 AC60 bars. This calculation fits quite well with the experimental observations as cracks in AC50 bars penetrate through the interlayer and in AC60 bars deflect along it. The critical porosity in this core/shell structure that gives an G^i_{IC}/G^f_{IC} of 0.25 is ~33%. This analysis also highlights the opportunity to achieve crack deflection by choosing a stiffness mismatch between the core and the matrix so that G^i_{IC}/G^f_{IC} becomes bigger and hence crack deflection happens in a less porous interlayer.

As cracks deflect along the cylindrical weak interlayers, they branch developing a tortuous path and rough fracture surfaces. These surfaces are quantitively examined as their increasing roughness is related to an increase in the proportion of Mode II fracture [43–46]. The roughness, R_a, of the fracture surfaces of AC60 is 145 μm, higher than for dense Al_2O_3 (25 μm) and AC50 (55 μm) bars (Fig. S7). This agrees with the stress-strain behavior and SEM observations, indicating that the weak interlayers developed in AC60 facilitates crack deflection and probably fiber pull out, improving the overall fracture resistance.

In addition, the fracture surfaces (Figs. 10 and 13(e)) suggest that AC60 Bouligand S has a crack twisting effect. This twist occurs as the crack deflects. We can provide a first approximation to the problem assuming Mode I loading and plane strain conditions. Although the crack path shows some deflection, at a macroscopic level we can identify a crack growing upwards from the notch (Fig. 7). Mode I loading has been used in previous published analysis of systems, enabling direct comparison [47–49]. Due to the relatively low K_{IC} (~ 3 MPa $m^{1/2}$) and high yield stress of alumina (above 1 GPa) [50,51], plain strain conditions are consistent with our sample dimensions. The fracture energy as a function of tilt angle (θ), $G(\theta)$, and twist angle (ϕ), $G(\phi)$, can be determined from: [52,53]

$$G(\theta) = K'^2_I(\theta)\left(1 - \upsilon^2\right)/E + K'^2_{II}(\theta)\left(1 - \upsilon^2\right)/E \tag{18}$$

$$G(\phi) = K'^2_I(\phi)\left(1 - \upsilon^2\right)/E + K'^2_{III}(\phi)(1 + \upsilon)/E \tag{19}$$

where the $K'_I(\theta)$, $K'_{II}(\theta)$, $K'_I(\phi)$ and $K'_{III}(\phi)$ are given by:

$$K'_I(\theta) = K_I\cos^3\left(\frac{\theta}{2}\right) \tag{20–1}$$

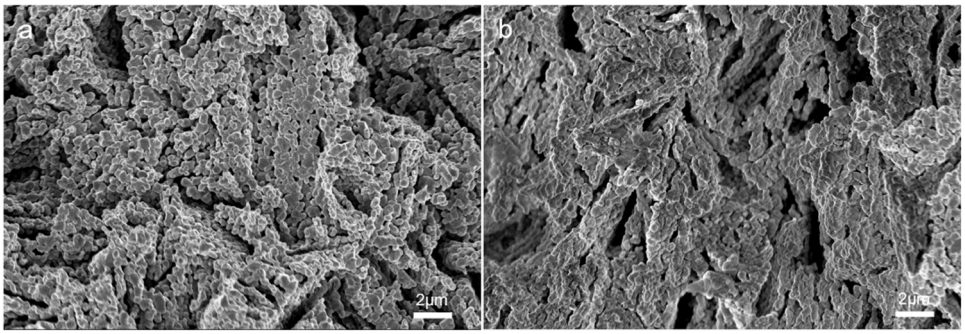

Fig. 12. SEM image of the interlayer in an (a) AC50 bar, (b) AC60 bar.

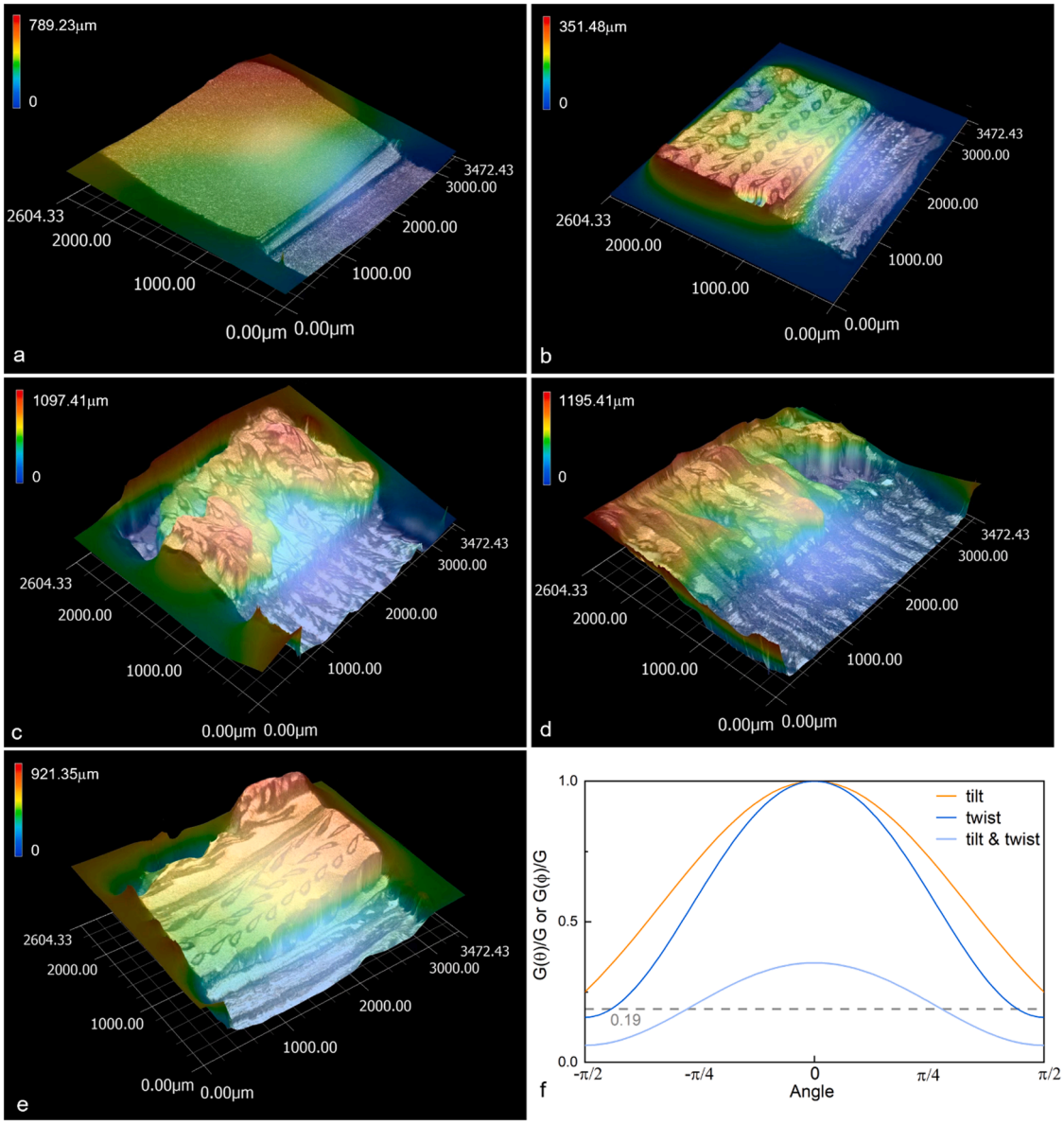

Fig. 13. (a–e) 3D profiles of fracture surface of (a)Al_2O_3, (b) AC50, length wise (c) AC60, length wise (d) AC60, Bouligand T alignment, (e) AC60, Bouligand S alignment, (f) the change of tilt (θ) and twist angle (ϕ) on reducing energy release rate for pure mode I loading. Plane strain assumed, with υ=0.2.

$$K_{II}^{'}(\theta) = K_I \sin\left(\frac{\theta}{2}\right)\cos^2\left(\frac{\theta}{2}\right) \tag{20–2}$$

$$K_I^{'}(\phi) = K_I^{'}(\theta)K_{11}(\phi) + K_{II}^{'}(\theta)K_{12}(\phi) \tag{20–3}$$

$$K_{III}^{'}(\phi) = K_I^{'}(\theta)K_{31}(\phi) + K_{II}^{'}(\theta)K_{32}(\phi) \tag{20–4}$$

$$K_{11}(\phi) = \cos^4\left(\frac{\theta}{2}\right)\left[2\upsilon\sin^2(\phi) + \cos^2\left(\frac{\theta}{2}\right)\cos^2(\phi)\right] \tag{20–5}$$

$$K_{12}(\phi) = sin^2\left(\frac{\theta}{2}\right)\cos^2\left(\frac{\theta}{2}\right)\left[2\upsilon\sin^2(\phi) + 3\cos^2\left(\frac{\theta}{2}\right)\cos^2(\phi)\right] \tag{20–6}$$

$$K_{31}(\phi) = \cos^4\left(\frac{\theta}{2}\right)\left[\sin(\phi)cos(\phi)\left(\cos^2\left(\frac{\theta}{2}\right) - 2\upsilon\right)\right] \tag{20–7}$$

$$K_{32}(\phi) = \sin^2\left(\frac{\theta}{2}\right)\cos^2\left(\frac{\theta}{2}\right)\left[\sin(\phi)cos(\phi)\left(3\cos^2\left(\frac{\theta}{2}\right) - 2\upsilon\right)\right] \tag{20–8}$$

The normalized values $G(\theta)/G$ and $G(\phi)/G$ are plotted in Fig. 13(f) using a Poisson's ratio for Al_2O_3 of ~0.2. Here the propagation of crack being purely tilting, purely twisting, a mixing of twist and tilt at a fixed tilt angle of 45° are presented. The crack will twist or tilt when the corresponding energy release rate ratio is above the ratio of fracture energies between the interlayer and the dense ceramic G_{IC}^{i}/G_{IC}^{f}. The latter ratio was calculated to be ~0.19. This means that when the tilt angle is 45°, the twist angle could range between −45° and 45°, indicating both tilting and twisting happen simultaneously. This corresponds to the observation of crack path in AC60 Bouligand S bars with a twisting and tilting angle are ~12° and ~42°, respectively.

It is interesting to note that crack deflection and twisting in AC60 appear when the filaments are close enough, allowing the bars function as a layered material. The interlayer doesn't affect the bending strength of the single extruded filaments because the tensile face is dense. Additionally, the strength of single filaments is twice that of bars (Fig. S2). This implies smaller critical defect sizes and suggests that defects trapped between lines may be limiting the strength of bars. These filaments fail catastrophically, whereas dense bars with proper weak interlayers exhibit progressive failure. Consequently, the mechanical

properties of whole bars could be possibly improved by selecting core materials with slightly greater fracture strain than the components [3,25].

There seems to be a size effect in the measurements of fracture resistance, as an increase in $K_{J,\ limit}$ is found in SENB samples with bigger size. Such an increase of toughness was also found in nacre-like ceramics where the $K_{J,\ limit}$ raised from 14.6 to 17.6 MPa·m$^{1/2}$ with increasing the sample size [54]. However, this may arise from the limitation of the testing method, only able to take into consideration the surface of the primary crack. In larger samples, it is more likely for a crack to initiate inside the material, generating a larger network of cracks. As such, the R-curve in Fig. 7i could overestimate K_J especially for big samples.

The strengths measured in this work are comparable to those reported for robocasted alumina (130–360 MPa) [33,55,56] and oxide fiber /oxide matrix composites (71–322 MPa) [57–59]. The fracture resistance is also in the range of those reported for oxide/oxide composites, for which the work of fracture ranges from 25 to 3200 J/m^2, and the toughness is 1–16 MPa·m$^{1/2}$, depending on the coating of the fibres and the density of the matrix [58–60].

Despite the positive change in fracture behavior and the increase in toughness achieved by introducing weak interlayers in dense Al_2O_3, there are some limiting factors. The weak interlayer is porous and serves as a defect close to the tensile surface. This has a slightly negative effect on strength and K_{IC}. A possible solution may be to replace the porous interlayer with a compliant material, such as the organic "mortar'' in nacre, small platelets or whiskers [13,14,22]. Alternatively, a tougher or less stiff core material could be used to still promote crack deflection with a less porous interlayer [19,20]. The contiguity of the weak interlayers was found to be critical in improving toughness by generations tortuous crack paths [3]. The weak interlayer in this work is continuous. However, cold isostatic pressing distorts the cross-section of the core-shell structure. The core and interlayer exhibit elliptical cross-sections in dense bars and the sharp corners could cause stress concentration. This issue could be addressed by using other 3D printing techniques like embedded 3D printing to print circular fiber arrays in a ceramic matrix [61]. Due to the limits in the size of the of nozzle tips used in robocasting, the filament diameters are of the order of hundreds of microns what hampers the fabrication of delicate structures at submicron and nanoscales. It is evident that as the dimension of the core-shell filaments becomes smaller, it is possible to add more layers of repeating structural units, that rotate from 0° to 180° per unit of thickness, enhancing crack deflection, twisting and delamination [18,24]. Changing the printing speed at a constant volumetric flow rate might be a feasible approach to tackle this restriction as it alters the dimension of the filaments and could be used to further introduce a dimensional gradient between and within layers.

5. Conclusion

In this work, a new strategy to improve the fracture resistance of alumina ceramics without the addition of any reinforcements or compliant phases was proposed by simply engineering a network of weak interlayers. This network was introduced during 3D printing, by co-extruding filaments with a core shell-structure in a robotic assisted deposition system. In these filaments, a carbon-ceramic interlayer separates the ceramic core and the shell. To achieve co-extrusion each component paste should be shear thinning with comparable viscosity during printing, shear thinning coefficient and velocity profile. Burning the carbon during sintering generates, porous and weak interlayers with plate-shaped pores aligned tangentially to the core. These interlayers can be used to direct crack propagation and their distribution is manipulated by controlling the printing direction. The presence of this weak interlayer enables an increase in toughness up to $K_J \approx 9$ MPa·m$^{1/2}$ from an initiation toughness, $K_{IC} \approx 3$ MPa·m$^{1/2}$, while maintaining the bending strength around 200 MPa. These results suggest that additive manufacturing can open new opportunities in the implementation of structural designs to direct crack propagation and generate fracture resistance.

Declaration of Competing Interest

The authors declare that they have no known competing financial interests or personal relationships that could have appeared to influence the work reported in this paper.

Acknowledgements

This work was supported by the EPSRC Program Manufacture Using Advanced Powder Processes (MAPP)EP/P006566. Shitong Zhou acknowledges financial assistance from the China Scholarship Council (No. 201806120001). We indebted to Professor Kang Li for accessing digital microscope.

Supplementary materials

Supplementary material associated with this article can be found, in the online version, at doi:10.1016/j.actamat.2023.118704.

References

[1] J.W. Halloran, Ceramic stereolithography: additive manufacturing for ceramics by photopolymerization, Annu. Rev. Mater. Res. 46 (1) (2016) 19–40.
[2] B.Y. Ahn, D. Shoji, C.J. Hansen, E. Hong, D.C. Dunand, J.A. Lewis, Printed origami structures, Adv. Mater. 22 (20) (2010) 2251–2254.
[3] R.P. Wilkerson, B. Gludovatz, J. Watts, A.P. Tomsia, G.E. Hilmas, R.O. Ritchie, A novel approach to developing biomimetic ("Nacre-Like") metal-compliant-phase (Nickel-Alumina) ceramics through coextrusion, Adv. Mater. 28 (45) (2016) 10061–10067.
[4] Y. Luo, D. Zhai, Z. Huan, H. Zhu, L. Xia, J. Chang, C. Wu, Three-dimensional printing of hollow-struts-packed bioceramic scaffolds for bone regeneration, ACS Appl. Mater. Interfaces 7 (43) (2015) 24377–24383.
[5] B.G. Compton, J.A. Lewis, 3D-printing of lightweight cellular composites, Adv. Mater. 26 (34) (2014) 5930–5935.
[6] B. Du, C. He, J. Qian, X. Wang, M. Cai, A. Shui, Ablation behaviors and mechanism of ultra-thick anti-oxidation layer coating on carbon-bonded carbon fiber composites, J. Am. Ceram. Soc. 102 (12) (2019) 7543–7552.
[7] P. Hu, S. Dong, X. Zhang, K. Gui, G. Chen, Z. Hu, Synthesis and characterization of ultralong SiC nanowires with unique optical properties, excellent thermal stability and flexible nanomechanical properties, Sci. Rep. 7 (1) (2017) 3011.
[8] S. Ghosh, S.T. Parker, X. Wang, D.L. Kaplan, J.A. Lewis, Direct-write assembly of microperiodic silk fibroin scaffolds for tissue engineering applications, Adv. Funct. Mater. 18 (13) (2008) 1883–1889.
[9] F. Bouville, E. Maire, S. Meille, B. Van de Moortele, A.J. Stevenson, S. Deville, Strong, tough and stiff bioinspired ceramics from brittle constituents, Nat. Mater. 13 (5) (2014) 508–514.
[10] S.E. Naleway, M.M. Porter, J. McKittrick, M.A. Meyers, Structural design elements in biological materials: application to bioinspiration, Adv. Mater. 27 (37) (2015) 5455–5476.
[11] J. Delage, E. Saiz, N. Al Nasiri, Fracture behaviour of SiC/SiC ceramic matrix composite at room temperature, J. Eur. Ceram. Soc. 42 (7) (2022) 3156–3167.
[12] D. Zhang, H. Yu, W. Wang, A. Wang, L. Ren, P. Hu, X. Zhang, D. Sun, Achieving synergy of load-carrying capability and damage tolerance in a ZrB2-SiC composite reinforced through discontinuous carbon fiber, J. Eur. Ceram. Soc. 41 (15) (2021) 7404–7411.
[13] T. Ohji, Y. Shigegaki, T. Miyajima, S. Kanzaki, Fracture resistance behavior of multilayered silicon nitride, J. Am. Ceram. Soc. 80 (4) (2005) 991–994.
[14] Y. Shigegaki, M.E. Brito, K. Hirao, M. Toriyama, S. Kanzaki, Processing of a novel multilayered silicon nitride, J. Am. Ceram. Soc. 79 (8) (1996) 2197–2200.
[15] G.J. Zhang, X.M. Yue, T. Watanabe, Al_2O_3/TiC/($MoSi_2$+Mo_2B_5) multilayer composites prepared by tape casting, J. Eur. Ceram. Soc. 19 (12) (1999) 2111–2116.
[16] W.J. Clegg, K. Kendall, N.M. Alford, T.W. Button, J.D. Birchall, A simple way to make tough ceramics, Nature 347 (6292) (1990) 455–457.
[17] Y. Yang, Z. Wang, Q. He, X. Li, G. Lu, L. Jiang, Y. Zeng, B. Bethers, J. Jin, S. Lin, S. Xiao, Y. Zhu, X. Wu, W. Xu, Q. Wang, Y. Chen, 3D printing of nacre-inspired structures with exceptional mechanical and flame-retardant properties, in: , 2022, 9840574, 2022.
[18] N. Suksangpanya, N.A. Yaraghi, R.B. Pipes, D. Kisailus, P. Zavattieri, Crack twisting and toughening strategies in Bouligand architectures, Int. J. Solids Struct. 150 (2018) 83–106.
[19] Y. Cheng, Y. An, Y. Liu, Q. Wei, W. Han, X. Zhang, P. Zhou, C. Wei, N. Hu, ZrB2-based "Brick-and-Mortar" composites achieving the synergy of superior damage tolerance and ablation resistance, ACS Appl. Mater. Interfaces 12 (29) (2020) 33246–33255.

[20] E. Feilden, C. Ferraro, Q. Zhang, E. Garcia-Tunon, E. D'Elia, F. Giuliani, L. Vandeperre, E. Saiz, 3D printing bioinspired ceramic composites, Sci. Rep. 7 (1) (2017) 13759.
[21] Y. Yang, X. Li, M. Chu, H. Sun, J. Jin, K. Yu, Q. Wang, Q. Zhou, Y. Chen, Electrically assisted 3D printing of nacre-inspired structures with self-sensing capability, Sci. Adv. 5 (4) (2019) eaau9490.
[22] V. Naglieri, B. Gludovatz, A.P. Tomsia, R.O. Ritchie, Developing strength and toughness in bio-inspired silicon carbide hybrid materials containing a compliant phase, Acta Mater. 98 (2015) 141–151.
[23] N. Zhao, M. Li, H. Gong, H. Bai, Controlling ice formation on gradient wettability surface for high-performance bioinspired materials, Sci. Adv. 6 (31) (2020) eabb4712.
[24] L.K. Grunenfelder, N. Suksangpanya, C. Salinas, G. Milliron, N. Yaraghi, S. Herrera, K. Evans-Lutterodt, S.R. Nutt, P. Zavattieri, D. Kisailus, Bio-inspired impact-resistant composites, Acta Biomater. 10 (9) (2014) 3997–4008.
[25] J. Mueller, J.R. Raney, K. Shea, J.A. Lewis, Architected lattices with high stiffness and toughness via multicore-shell 3D printing, Adv. Mater. 30 (12) (2018), e1705001.
[26] T. Schlordt, S. Schwanke, F. Keppner, T. Fey, N. Travitzky, P. Greil, Robocasting of alumina hollow filament lattice structures, J. Eur. Ceram. Soc. 33 (15–16) (2013) 3243–3248.
[27] Y.W. Moon, I.J. Choi, Y.H. Koh, H.E. Kim, Macroporous alumina scaffolds consisting of highly microporous hollow filaments using three-dimensional ceramic/camphene-based co-extrusion, J. Eur. Ceram. Soc. 35 (16) (2015) 4623–4627.
[28] Q. Cai, Robocasting of Complex Structural Ceramics, Department of Materials, Imperial College London, 2020.
[29] Q. Cai, S. Meille, J. Chevalier, S. Zhou, F. Bouville, I. Tirichenko, E. Saiz, 3D-printing of ceramic filaments with ductile metallic cores, Mater. Des. 225 (2023).
[30] Z. Fu, M. Freihart, T. Schlordt, T. Fey, T. Kraft, P. Greil, N. Travitzky, Robocasting of carbon-alumina core-shell composites using co-extrusion, Rapid Prototyp. J. 23 (2) (2017) 423–433.
[31] C. Paredes, F.J. Martínez-Vázquez, A. Pajares, P. Miranda, Novel strategy for toughening robocast bioceramic scaffolds using polymeric cores, Ceram. Int. 45 (15) (2019) 19572–19576.
[32] Y. Xia, Z. Lu, J. Cao, K. Miao, J. Li, D. Li, Microstructure and mechanical property of Cf/SiC core/shell composite fabricated by direct ink writing, Scr. Mater. 165 (2019) 84–88.
[33] E. Feilden, E.G.T. Blanca, F. Giuliani, E. Saiz, L. Vandeperre, Robocasting of structural ceramic parts with hydrogel inks, J. Eur. Ceram. Soc. 36 (10) (2016) 2525–2533.
[34] W.H. Herschel, R. Bulkley, Konsistenzmessungen von gummi-benzollösungen, Kolloid Z. 39 (4) (1926) 291–300.
[35] A. M'Barki, L. Bocquet, A. Stevenson, Linking rheology and printability for dense and strong ceramics by direct ink writing, Sci. Rep. 7 (1) (2017) 6017.
[36] J.E. Smay, J. Cesarano, J.A. Lewis, Colloidal inks for directed assembly of 3-D periodic structures, Langmuir 18 (14) (2002) 5429–5437.
[37] A.K. Grosskopf, R.L. Truby, H. Kim, A. Perazzo, J.A. Lewis, H.A. Stone, Viscoplastic matrix materials for embedded 3D printing, ACS Appl. Mater. Interfaces 10 (27) (2018) 23353–23361.
[38] S.M. Peker, S.S. Helvaci, Solid-Liquid Two Phase Flow, Elsevier, 2011.
[39] R.O. Ritchie, The conflicts between strength and toughness, Nat. Mater. 10 (11) (2011) 817–822.
[40] A. International, Standard Practice for Fractography and Characterization of Fracture Origins in Advanced Ceramics, ASTM International, 2019.
[41] T. Ostrowski, J. Rödel, Evolution of mechanical properties of porous alumina during free sintering and hot pressing, J. Am. Ceram. Soc. 82 (11) (1999) 3080–3086.
[42] H. Ming-Yuan, J.W. Hutchinson, Crack deflection at an interface between dissimilar elastic materials, Int. J. Solids Struct. 25 (9) (1989) 1053–1067.
[43] A.R. Boccaccini, V. Winkler, Fracture surface roughness and toughness of Al_2O_3-platelet reinforced glass matrix composites, Compos. Part A Appl. Sci. Manuf. 33 (1) (2002) 125–131.
[44] M. Moreira Arouche, S. Teixeira de Freitas, S. de Barros, On the influence of glass fiber mat on the mixed-mode fracture of composite-to-metal bonded joints, Compos. Struct. 256 (2021).
[45] C. Li, D. Yang, H. Xie, L. Ren, J. Wang, Research on the anisotropic fracture behavior and the corresponding fracture surface roughness of shale, Eng. Fract. Mech. 255 (2021).
[46] T.V. Le, A. Ghazlan, T. Ngo, T. Nguyen, Performance of a bio-mimetic 3D printed conch-like structure under quasi-static loading, Compos. Struct. 246 (2020).
[47] G.X. Gu, M. Takaffoli, M.J. Buehler, Hierarchically enhanced impact resistance of bioinspired composites, Adv. Mater. 29 (28) (2017).
[48] L.Roy Xu, Y.Y. Huang, A.J. Rosakis, Dynamic crack deflection and penetration at interfaces in homogeneous materials: experimental studies and model predictions, J. Mech. Phys. Solids 51 (3) (2003) 461–486.
[49] S. Strobl, P. Supancic, T. Lube, R. Danzer, Surface crack in tension or in bending – a reassessment of the Newman and Raju formula in respect to fracture toughness measurements in brittle materials, J. Eur. Ceram. Soc. 32 (8) (2012) 1491–1501.
[50] S. Korte, W.J. Clegg, Micropillar compression of ceramics at elevated temperatures, Scr. Mater. 60 (9) (2009) 807–810.
[51] K.P.D. Lagerlof, A.H. Heuer, J. Castaing, J.P. Riviere, T.E. Mitchell, Slip and twinning in sapphire (alpha-Al_2O_3), J. Am. Ceram. Soc. 77 (2) (1994) 385–397.
[52] B.R. Lawn, Fracture of Brittle Solids, 2nd ed., Cambridge University Press, Cambridge, 1993.
[53] K.T. Faber, A.G. Evans, Crack deflection processes – I. theory, Acta Metall. 31 (4) (1983) 565–576.
[54] H. Saad, K. Radi, T. Douillard, D. Jauffres, C.L. Martin, S. Meille, S. Deville, A simple approach to bulk bioinspired tough ceramics, Materialia 12 (2020).
[55] I.S. Elizarova, L. Vandeperre, E. Saiz, Conformable green bodies: plastic forming of robocasted advanced ceramics, J. Eur. Ceram. Soc. 40 (2) (2020) 552–557.
[56] L. Rueschhoff, W. Costakis, M. Michie, J. Youngblood, R. Trice, Additive manufacturing of dense ceramic parts via direct ink writing of aqueous alumina suspensions, Int. J. Appl. Ceram. Technol. 13 (5) (2016) 821–830.
[57] T.J. Pirzada, D. Liu, J. Ell, H. Barnard, I. Šulák, M. Galano, T.J. Marrow, R. O. Ritchie, *In situ* observation of the deformation and fracture of an alumina-alumina ceramic-matrix composite at elevated temperature using x-ray computed tomography, J. Eur. Ceram. Soc. 41 (7) (2021) 4217–4230.
[58] K.K. Chawla, C. Coffin, Z.R. Xu, Interface engineering in oxide fibre/oxide matrix composites, Int. Mater. Rev. 45 (5) (2013) 165–189.
[59] E. Volkmann, K. Tushtev, D. Koch, C. Wilhelmi, J. Göring, K. Rezwan, Assessment of three oxide/oxide ceramic matrix composites: mechanical performance and effects of heat treatments, Compos. Part A Appl. Sci. Manuf. 68 (2015) 19–28.
[60] X. Li, X. Fan, N. Ni, X. Zhao, C. Li, P. Xiao, Continuous alumina fiber-reinforced yttria-stabilized zirconia composites with high density and toughness, J. Eur. Ceram. Soc. 40 (4) (2020) 1539–1548.
[61] S. Zhou, I.S. Elizarova, X. Zhang, Y. Hong, H. Payne, P. Withers, F. Bouville, E. Saiz, Embedded 3D printing of multi-material composites, 19 October 2022, PREPRINT (Version 1) available at Research Square (https://doi.org/10.21203/rs.3.rs-2151613/v1).